

Pressure and Strain Measurement on an Inclined Flap in Supersonic Flow using a Dual-Layer Luminescent Coating

Amruthkiran Hegde¹, Garrett Sellers¹, Semih M. Ölçmen² and James P. Hubner² *The University of Alabama, Tuscaloosa, AL 35487-0280*

This paper reports the progress to combine two coating techniques—pressure-sensitive paints (PSPs) and photoelastic coatings (PECs) to measure full-field, dynamic pressure and strain fields. The technique applies a Fast-PSP onto the surface of a PEC adhered to the test specimen. A dual LED approach is used to overcome poor polarization retention of the PSP luminophor. The theory of the technique is presented and results for a cantilever specimen placed within a pressure chamber and driven near resonant frequency are discussed. Preparation and initial results of a demonstration on a 12° flap in Mach 3 flow are also presented as the technique is extended to high-speed aerodynamic environments.

Nomenclature

Variables			Abbreviations		ons
а	=	coating absorptivity	DL	=	dual-layer
A, B	=	PSP calibration coefficients	LP	=	linear polarizer
F,G	=	amplitude and phase of optical strain response	LPC	=	luminescent photoelastic coating
h	=	coating thickness	LPF	=	long-pass filter
I	=	emission intensity	OSR	=	optical strain response
I_{ref}	=	reference emission intensity	PEC	=	photoelastic coating
K	=	photoelastic coating sensitivity	PSP	=	pressure-sensitive paint
L	=	length of beam (clamp to free end)	QWP		quarter-wave plate
N	=	fringe order	_		
P	=	pressure			
P_{ref}	=	reference pressure			
t	=	time			
α	=	analyzer angle, or flow reattachment angle			
β	=	oblique shock angle			
γ	=	maximum in-plane shear strain			
δ	=	flap angle			
ε_i	=	principal strains			
θ	=	principal strain direction			
λ	=	wavelength			
λ^*	=	effective excitation-emission wavelength			
λ_{em}	=	emission wavelength			
λ_{ex}	=	excitation wavelength			
ν	=	Poisson ratio			
σ	=	standard deviation			
ϕ	=	polarization efficiency			

¹ Graduate Student, Aerospace Engineering and Mechanics.

² Professor, Aerospace Engineering and Mechanics, AIAA Associate Fellow.

I. Introduction

Validation of unsteady theoretical and computational fluid-structure interaction models for flight technologies and systems, particularly pressure fluctuations, requires high temporal and spatial resolution data and corresponding measurement techniques. Acquisition of this data is often compromised by traditional surface and off-surface probes that can interfere and distort the airflow, necessitating substantial correction techniques. Pointwise techniques such as pressure taps, accelerometers, and strain gauges, while highly accurate, can have insufficient spatial resolution or add significant time and cost to instrument the model.

This paper presents the progress towards integrating two full-field, optical sensor techniques to measure the unsteady, distributed loads (pressure), and strains on aerodynamically-induced vibrating or deforming surfaces, with the goal to extend into high-speed flows. The approach is to combine fast-response pressure-sensitive paints with thin photoelastic coatings to create a fast luminescent pressure and strain measurement technique. The average emission intensity, I_{avg} , and amplitude intensity, I_{amp} , for camera pixels sensitive to polarization (Fig. 1) is hypothesized to be sensitive to the pressure, P, and maximum in-plane shear strain, γ , respectively.

In this paper, progress on two experiments is presented. First, pressure and strain measurements of a cantilever beam specimen driven at frequencies to induce a dynamic stress/strain field are presented. The specimens are placed in a pressure-controlled environment. This is a continuation of prior bench-top testing and validation of the technique [1]. Second, preparation to implement the technique on an inclined flap in Mach 3 flow will be presented. The inclined flap configuration is a simple, generic geometry that is similar to an air vehicle control surface. In supersonic flows, these surfaces may be exposed to phenomena such as shock-shock and shockwave-boundary layer interactions (SWBLI). These phenomena can lead to dynamic pressure and deformation fields arising from transient mechanical loads due to oscillating shock fronts and separating vortices that can potentially couple with structural resonant frequencies.

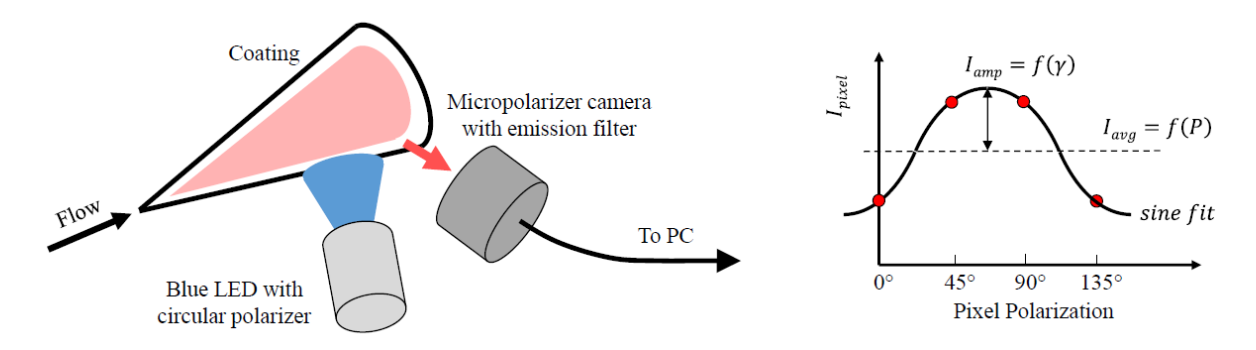


Figure 1. Schematic of fast pressure and strain measurement system: each camera superpixel is sensitive to one of four polarization states. Average and amplitude intensity are hypothesized to be sensitive to pressure, P, and strain, γ , respectively.

II. Background and Theory

A. Pressure-Sensitive Paints

The pressure-sensitive paint technique (PSP) [2] has become a common measurement technique in the aerodynamic community and successful implementation of fast pressure-sensitive paints (Fast-PSP) have followed due to improvements in paint formulations, ultra-bright light-emitting diodes (LEDs) and high-quantum-efficiency, high-speed digital cameras. A typical PSP is composed of two parts: an oxygen-sensitive fluorescent molecule and an oxygen permeable binder. When a luminescent molecule absorbs a photon of appropriate wavelength, it transitions to an excited energy state. The molecule then typically recovers to the ground state by the emission of a longer-wavelength photon (loss of energy due to thermal relaxation). In some materials, oxygen can interact with the molecule such that the transition to the ground state is non-radiative; this process is known as oxygen quenching. The rate at which these two processes compete is dependent on the partial pressure of oxygen, with a higher oxygen pressure increasing the quenching of the molecule and decreasing the measured luminescence.

Image-based pressure measurements using PSP are accomplished by coating the model surface with the paint and illuminating the surface with light of the appropriate wavelength (usually in the UV to blue range) to excite the luminescent molecules within the coating. The surface is imaged through a bandpass or long-pass filter (LPF) to separate the luminescent signal from the excitation light. The luminescent signal from the paint is not only a function of pressure but also varies with illumination intensity, probe concentration, paint layer thickness, and detector sensitivity. These spatial variations result in a non-uniform intensity map from the painted surface. The spatial variations are usually eliminated by taking the ratio of the luminescent intensity of the PSP at an unknown test condition, I, and a known reference condition, I_{ref} . Most PSPs are modeled following the linear Stern-Volmer relationship [2], as shown in Eq. 1

$$\frac{P}{P_{ref}} = A + B \frac{I_{ref}}{I},\tag{1}$$

a second order polynomial, or a nonlinear dual-sorption model. For Eq. 1, A and B are temperature dependent coefficients and P is pressure.

Conventional PSP formulations typically use a polymer as a binder material. Polymer binders enable the diffusion of oxygen into the embedded dye molecules. The response time of the paint is largely governed by the rate of oxygen diffusion into the binder which is proportional to the thickness squared and inversely proportional to the binder diffusivity. Thick, conventional formulations have response times on the order of a second. Decreasing the coating thickness to improve response time has the disadvantage of sacrificing luminescent output and signal-to-noise ratio. Porous PSPs use highly porous binders, enhancing the oxygen diffusion and improving the temporal response characteristics. The drawback of a porous PSP is nearly complete quenching at low pressures. Hybrid paint formulations use ceramic particles in the paint, creating a porous structure that decreases the effective thickness, increases the effective diffusivity and extends the pressure range. This results in a fast-response system with favorable signal-to-noise ratio. Hybrid PSP formulations can detect pressure fluctuations up to 20 kHz, and unsteady pressure measurements have been demonstrated on a variety of models [3-6]. Fast-PSP has also been paired with stereo-photogrammetry techniques to measure pressure and deformation [7].

B. Photoelastic Coatings

Photoelastic coatings (PEC) [8] have been used in the structural testing community for many years, primarily for static testing but applicable to dynamic testing related to stress wave propagation and impact [9]. The dynamic response of photoelastic coatings is high due to the propagation of wave speeds through the thin coatings. Typical PEC density and elastic modulus are approximately $1000 \ kg/m^3$ and $1 \ GPa$, respectively. For a $1 \ mm$ thick coating, the theoretical response time based on wave propagation would be approximately $1 \ \mu s$.

Photoelastic coatings work on the principle of birefringence: the ability of a material to transmit light at different velocities relative to the polarization and propagation of the incoming light. In application, a reflective photoelastic coating is adhered to the surface of the model of interest and illuminated with circular polarized light (a combination of a linear polarizer (LP) and achromatic quarter-wave plate (QWP) rotated 45° relative to the polarizer). The stress induced change in the polarization as light passes into and reflects out of the coating is measured using a second linear polarizer, often called an analyzer \S , and a camera. As with all birefringent coatings, the change in polarization is related to the maximum shear strain, γ , in the plane perpendicular to the path of the polarized light passing through the specimen. To quantify the strain field, a sequence of images at different analyzer angles is necessary. The development of micropolarizer masks attached to the imager chip eliminates the need of an exterior rotating analyzer and allows multiple analyzer states, typically four, to be acquired with each image. This is an important advancement for dynamic applications.

The luminescent photoelastic coating (LPC) technique [11, 12] consists of a luminescent dye in, on or underneath a photoelastic binder. The luminescence creates a more uniform emission field at oblique incidence compared to the reflected field of traditional reflective photoelastic coatings. This higher relative signal on oblique surfaces enables the potential of principal strain separation [13]. The emission intensity of an LPC after it passes through the analyzer is characterized by Eq. 2 [11],

[§] This configuration is sometimes referred to a greyscale polariscope [10]. A more traditional configuration combines a quarter-wave plate and polarizer in front of the imager [8].

$$\frac{I_{\alpha}}{I_{avg}} = 1 + Fsin(2\alpha - 2G), \qquad (2)$$

where I_{α} is the emission intensity at a pixel for a specific analyzer (or micropolarizer) orientation, I_{avg} is the average measured emission intensity over 180° analyzer rotation, α is the analyzer (or micropolarizer) angle, F is the magnitude of the optical strain response (OSR, shown as I_{amp} in Fig. 1) and G is the phase of the OSR. The phase is related to the principal strain direction relative to the 0° analyzer (or pixel) angle. The OSR is a function of the inplane maximum shear strain, γ . For a single-layer LPC with both a luminescent dye for strain detection and an absorption dye for thickness independence [11], the OSR is

$$F = \phi \frac{\gamma/\eta}{1 + (\gamma/\eta)^2}, \qquad \eta = \frac{a\lambda^*}{2\pi K}, \tag{3}$$

where ϕ is the polarization-retention efficiency of the luminescence and η is the coating characteristic, which is a function of the absorptivity, a, the coating optical sensitivity, K, and the effective excitation-emission wavelength, λ^* :

$$\lambda^* = \frac{\lambda_{ex}\lambda_{em}}{\lambda_{ex} + \lambda_{em}}. (4)$$

The polarization efficiency depends on the ability of the luminescent process to retain the state of excitation polarization after emission. The optical sensitivity is a material property of the coating. If there is no absorption dye in the coating, the luminescent intensity increases and the OSR is [14]

$$F = \phi \frac{1 - \cos(\gamma/\eta)}{\gamma/\eta}, \qquad \eta = \frac{\lambda^*}{2\pi h K}, \tag{5}$$

where h is the thickness of the coating.

A dual-layer (DL) coating with a single LED excitation source places the luminescent dye above the PEC ($\lambda^* = \lambda_{em}/2$, double-pass of emission through the coating) or below ($\lambda^* = \text{Eq. 4}$). For these two cases, the polarized emission intensity is

$$F = \phi \sin\left(\frac{\gamma}{\eta}\right), \qquad \eta = \frac{\lambda^*}{2\pi h K}.$$
 (6)

Figure 2 compares theoretical OSR for the coating with an absorption dye, without absorption dye and with the luminescent dye above the coating for $\phi = 1$. The polarization efficiency and coating characteristic are determined through *in situ* or *a priori* calibration. While the latter is easier to implement if known, the former is more accurate, assisting in the elimination of systematic errors that can arise from batch variance, surface reflectance, optical interference and environmental dependencies. The retention of polarization during luminescence depends on the type of luminophor and its concentration, and the polarization efficiency will be less than one.

The coating characteristic, η , can be thought of as a characteristic strain value that affects the curvature and sensitivity of the OSR amplitude. A larger coating characteristic decreases the OSR sensitivity but extends its range. This is important to reduce the difficulty in determining a unique solution for the strain. For strain values beyond the first OSR peak of $\gamma \ge \eta \pi/2$, the relationship is multi-valued requiring fringe counting and phase-

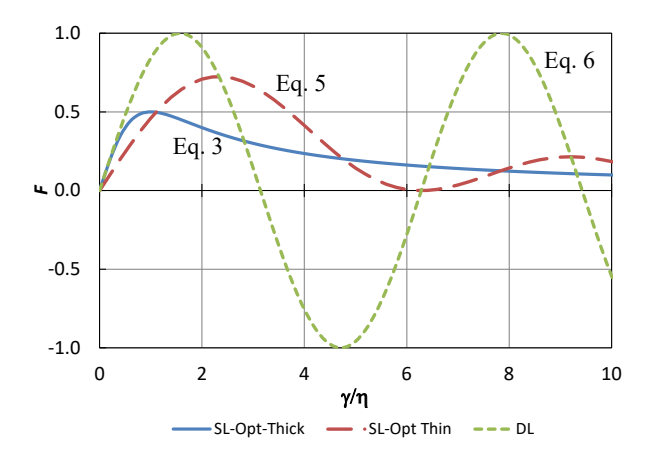


Figure 2. Optical strain response, *F*, of a single-layer coating with absorption dye (blue solid line, Eq. 3), single-layer coating without absorption dye (red dash line, Eq. 5), and dual-layer coating (green dotted line, Eq. 6)

unwrapping techniques. There are multiple approaches to extend OSR range: decrease the coating thickness, use a PEC with lower optical sensitivity, K, or increase the effective wavelength. The latter approach would be the most difficult as it depends on the absorption and emission properties of the luminescent coating.

C. Combined Technique

The initial approach to combine the two techniques was to use a DL coating. The luminescence of the PSP (top layer) would pass through the PEC (bottom layer) [1]. The DL coating would be excited by a single UV/blue LED with LP/QWP optics. Pressure changes would quench the PSP emission and strain changes would alter the emission polarization as it passed through the PEC and reflected towards the imager. This approach requires the PSP coating luminescence to partially retain the polarization of the excitation to be able to detect the strain-induced birefringence. The advantage of this approach is a single excitation source and synchronized pressure and strain detection. The efficiency of polarization retention for the Fast PSP, however, proved to be low compared to luminophors designed for LPCs that do not require oxygen quenching, resulting in poor strain resolution and long exposure times (>100 ms) [1].

Thus, an alternative method presented in this paper is a two-LED approach: a UV/blue LED without polarization optics used to excite the PSP (pressure response) and a red LED with polarization optics (LP/QWP pair) used to detect stress-induced polarization of the PEC (strain response). The main cost of the two-LED approach is alternating pressure and strain measurements (images). This downside, though, is outweighed by a strong strain-dependent signal and faster acquisition rates afforded by pairing the polarization optics on the red LED. Because the PEC response is based on light reflection as opposed to the PSP response, which is light emission, the PEC requires a less powerful LED. Thus, it is preferred to pair the polarization optics on the red LED.

Figure 3 is a schematic of the two LED approach. The PSP is applied on top of the PEC. The camera and two LEDs are triggered with an external source. The camera is triggered at twice the frequency of the LEDs. The LEDs are triggered 180° out-of-phase with each other, and their duty cycle is less than 50% to synchronize with the camera exposure time. An LPF is necessary to block the UV/blue excitation and allow the PSP emission and the PEC reflection to pass through to the imager. The light is imaged through a pixelated polarizer mask on the digital camera. Each pixel measures an intensity relative to the polarization orientation of that pixel. A typical micropolarizer array has four discrete orientations in a 2×2 pattern: $0/45/90/135^{\circ}$. The group of four pixels is called a superpixel.

The PSP emission and PEC reflection intensities recorded by each pixel are dependent on pressure, strain, excitation intensity, and coating thickness/concentration. Like [1], the pressure information is tracked by the average of the four pixel intensities (assuming strain-independence), and the strain information is modeled by the variance of the pixel intensities (assuming pressure-independence). However, the information is separated into alternating blue and red LED pulses. For a superpixel exposed to the blue LED,

$$I_{b,avg} = \overline{I_b} = \frac{(I_0 + I_{45} + I_{90} + I_{135})}{4} \neq f(\gamma)$$
 (7)

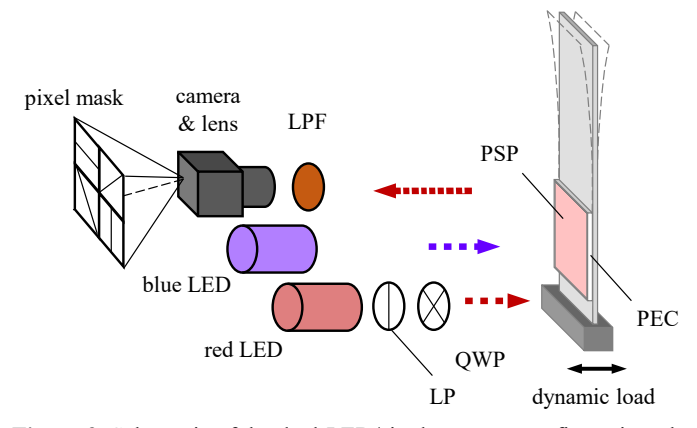


Figure 3. Schematic of the dual-LED/single-camera configuration; the red and blue LEDs are pulsed out-of-phase with each other

In terms of the Stern-Volmer pressure response (blue LED image),

$$\frac{\overline{I_{b,ref}}}{\overline{I_b}} = A + B \frac{P}{P_{ref}}.$$
 (8)

The strain response for the two-layer coating exposed to the red LED is modeled by

$$\frac{I_{r,\alpha}}{I_{r,\alpha}} = 1 + \sin\left(\frac{\gamma}{\eta}\right) \sin(2\alpha - 2G) , \qquad (9)$$

where $I_{r,\alpha}$ is the intensity of each pixel for $\alpha=0/45/90/135^\circ$. Polarization efficiency is assumed to be $\phi=1$ as the PEC response is not based on PSP luminescence but instead reflection of the polarized red LED illumination. Relative to the pixel orientation, α , the measured intensity follows a sinusoidal curve $\sin(2\alpha-2G)$. The amplitude of the corresponding curve fit, or the OSR, is $\sin(\gamma/\eta)$. A reference state is not required because the variance across the four pixels is compared to the average of the four pixels, $\overline{I_{r,\alpha}}$. To calculate OSR and the phase, and hence strain and principal direction, a non-linear fit algorithm such as the Levenberg-Marquart routine is suitable. Alternatively, and more computationally efficient, the standard deviation of $\frac{I_{r,\alpha}}{I_{r,\alpha}}$ for a superpixel can be used,

OSR =
$$\sin\left(\frac{\gamma}{\eta}\right) = \sqrt{\frac{n-1}{n}} \operatorname{stdev}\left(\frac{I_{r,\alpha}}{I_{r,\alpha}}\right),$$
 (10)

where n is the number of evenly spaced pixel orientations (in this case n = 4). To calculate the phase,

$$2G = \operatorname{atan2}\left(\frac{I_0 - I_{90}}{I_{45} - I_{135}}\right). \tag{11}$$

In cases where the strain is zero or at a fringe node, the intensity ratio is constant with respect to analyzer orientation and OSR = 0. If the OSR is not zero at the reference state (e.g., residual birefringence in the coating), then a vector subtraction of the residual state is necessary [15].

When calculating the corresponding strain from the measured OSR, multiple strain values could result. This requires fringe counting or phase unwrapping. By limiting the coating thickness to less than a quarter-fringe, then fringe counting is eliminated. The fringe order, N, is

$$N = \frac{\gamma}{2\pi\eta} \ . \tag{12}$$

This corresponds to $N < \frac{1}{4}$ or $\gamma_{max} < \frac{\lambda^*}{4hK}$ as well as knowledge *a priori* of the expected maximum shear strain.

III. Benchtop Test Apparatus

Figure 4 is an image of the benchtop pressure and shake chamber used in this investigation. To excite the PSP, an air-cooled ISSI LM3X 400 nm (blue) 36 W LED lamp is used. To illuminate the PEC, an ISSI LM2 620 nm (red) 4 W LED lamp is used. Aligned in the red LED excitation path is an LP and an achromatic QWP, rotated at 45° relative to the polarizer, to create circular polarized red light. The imager is a 4D-Technologies PolarCam U2 CMOS camera with a 0/45/90/135° linear polarization mask for each superpixel. The maximum full-field frame rate is

164 fps at 12-bit, but higher frames rates are possible for smaller and rotated regions of interest. Attached to the camera is a Nikon 50 mm lens set at an f-stop of 1.2. A 450 nm reflective LPF and 570 nm Schott glass LPF is attached to the lens.

National Instruments data acquisition hardware is used to trigger the LEDs and camera (NI-9237 module) and record calibrating strain gage measurements (NI-9263 module). The LEDs are triggered alternatively at half the rate of the camera and a 45% duty-cycle. This enables the camera to alternatively capture pressure (blue) and strain (red) signals. Triggering and strain gage recording are performed with in-house LabVIEW virtual instruments (VIs). *Polarcam* software [16], provided by 4D Technologies, is used to control the camera when focusing the image, establishing appropriate exposure times, and tuning (rotating) the QWP to create circular polarized excitation. *eBus Player* software is used to control the camera and set parameters in trigger mode.

The specimens are thin aluminum (6061-T6) cantilever beams. The pressure and shake chamber, Fig. 4, can accommodate specimens $1-3 \, mm$ thick, $20-30 \, mm$ wide and $260 \, mm$ long. The chamber can control the pressure between $10 \, kPa$ to $101 \, kPa$. A new glass window was designed and fabricated to replace a thicker acrylic window. The glass window decreases the photoelastic interference created when the window is stressed by sub-atmospheric pressure.

For this investigation, specimens are $25.4 \, mm \times 254 \, mm$, with thickness of $1.6 \, mm$ (thin) or $2.3 \, mm$ (thick). The beams are clamped at one end and sinusoidally driven using a shaker rod passing through the chamber's backside and connecting to the beam mount (Fig. 5). The shaker frequency and amplitude are set by an external function generator and pre-amplifier. Based on the thickness and clamped length of the beam, resonance can be controlled. The fundamental resonant frequencies of the thin and thick beams are $22 \, \text{and} \, 32 \, Hz$, respectively. Due to inertial acceleration, the induced stress in the cantilever specimen will decrease from the base to the free end. The principal stress aligns along the length of the beam, and the corresponding maximum inplane shear strain is $\gamma = \varepsilon_1 - \varepsilon_2 = (1 + \nu)\varepsilon_1$.

A 76 mm \times 25.4 mm strip of PEC (Micro-Measurement PS-1; h=0.51 mm, K=0.15) is adhered with PC-10 reflective adhesive near the clamped end of the specimen. Next, a layer of water-based, porous polymer is sprayed on the surface to the PEC. The polymer underlayer assists in protecting the PEC from the solvents of the PSP layer. Finally, a thin layer of PtTFPP-PP Fast-PSP [17] is sprayed on the surface of the polymer. The center absorption band of the PSP is 400 nm, and the center emission band is 650 nm. Thin layering of the PSP allows 620 nm excitation of the red LED to reach the PEC. The theoretical coating characteristic, η , is 645 $\mu\varepsilon$. A uni-axial resistive strain gage is adhered to the back side of the specimen to record the time-dependent strain profile.

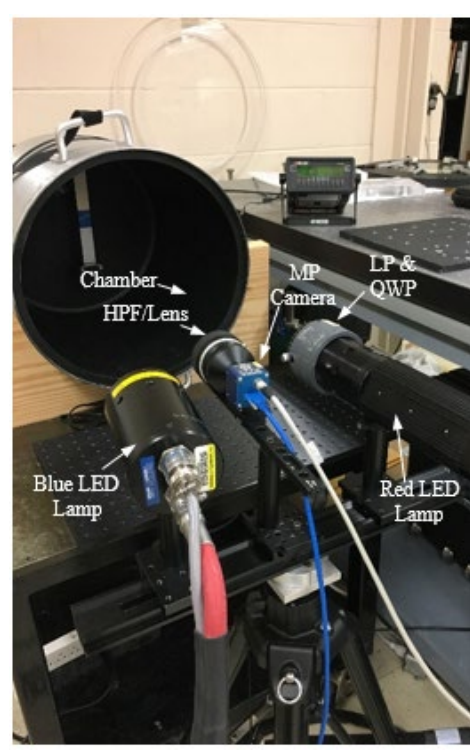


Figure 4. PSP/PEC test apparatus

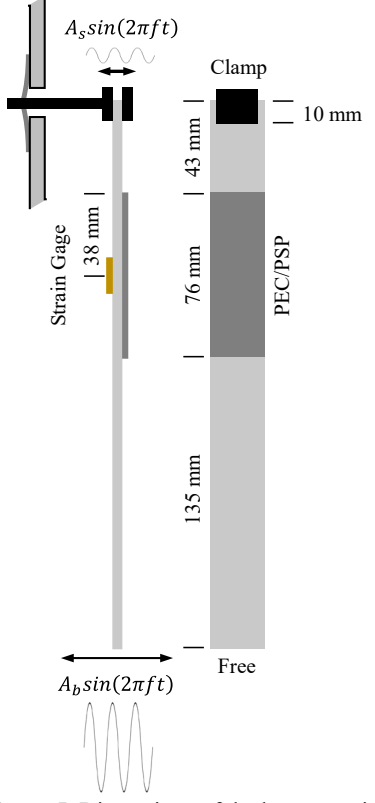


Figure 5. Dimensions of the beam specimen

IV. Benchtop Calibration Test: Results and Discussion

The thick beam specimen was excited at $23.5 \, Hz$, lower than the fundamental frequency, to limit the maximum induced strain. The camera was triggered at $200 \, Hz$. Pixel density was 5.9/mm. Data was acquired at four chamber pressure ratios: 0.20, 0.41, 0.61 and 1.00. Image post-processing included flat-field correction, dark image correction, four-point affine image registration, 15×15 median smoothing filter and zero-load OSR correction. The effects of registration and filtering on a pressure ratio image, and subsequent improvements, are shown in Fig. 6.

Pressure response: Figure 7 is a plot of the intensity ratio $\overline{I_{b,ref}}/\overline{I_b}$, OSR, and phase (G) recorded with unpolarized blue LED excitation at $P/P_{ref} = 0.02$. The reference state is atmospheric pressure and at rest (i.e., no load). Images

from left to right represent time steps of 10 ms. The intensity ratio (top row; proportional to the average of the superpixel) is approximately constant across the field of view $(\overline{I_{b,ref}}/\overline{I_b} = 0.33)$, showing no measurable strain interference or pressure effects due to the oscillation. The OSR (middle row; proportional to the standard deviation of the superpixel relative to the average of the superpixel) is near zero as expected as the blue LED excitation is unpolarized, thus the intensities in the four pixels are approximately equal within the noise band. The phase plot (bottom row; indication of principal strain direction) is scattered, ranging between 0 and $\pm \pi/2$. This too is expected as the calculated phase is based on intensity difference of the pixels, which is the noise band (again, unpolarized excitation). The splotchy nature of the phase plot is a remnant of median filter kernel size. Figure 8 (left) compares the intensity ratio at the four different pressure ratios. Figure 8 (right) is the corresponding Stern-Volmer plot. Similar to Fig. 7, the strain field is not visibly present in the emission intensity ratio from the unpolarized blue LED.

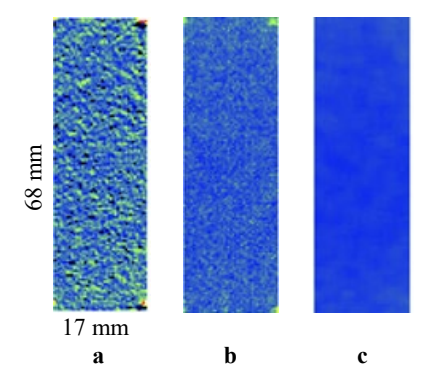


Figure 6. Intensity ratio contour for $P/P_{ref} = 0.2$: a) no registration, b) with registration, c) with registration and smoothing filter

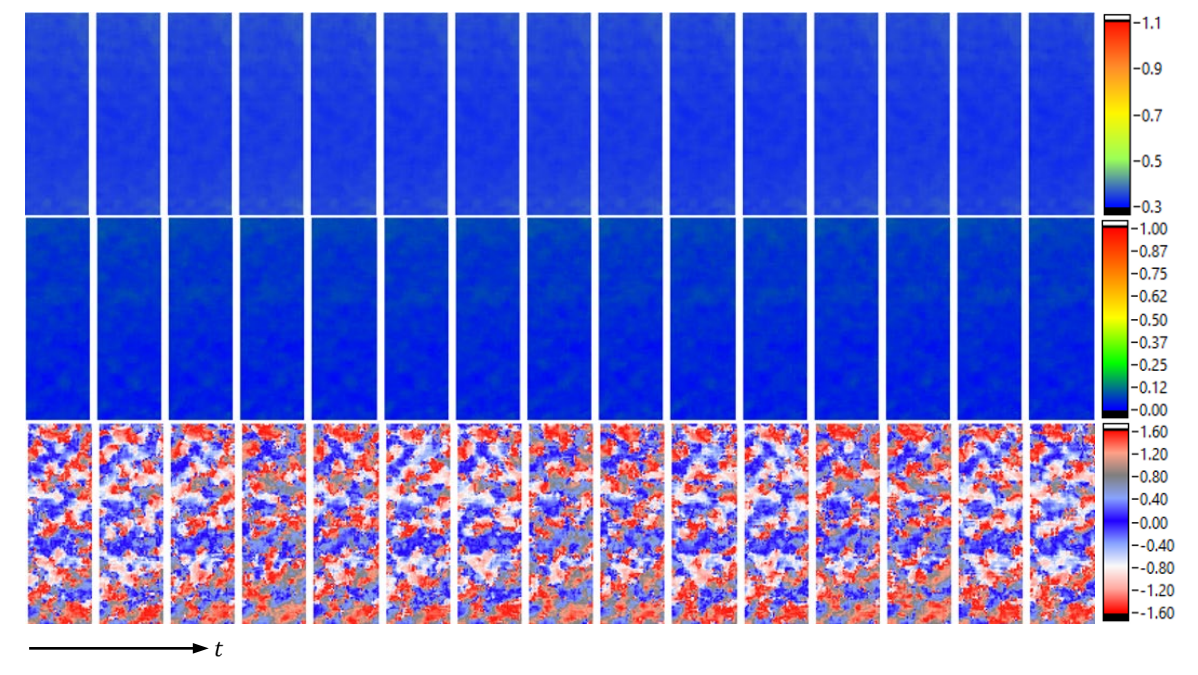


Figure 7. Intensity ratio $\overline{I_{b,ref}}/\overline{I_b}$ (top row), OSR (middle row), and phase G (bottom row; radians) recorded for the unpolarized blue LED excitation at $P/P_{ref} = 0.20$: thick beam driven at 23.5 Hz, images from left to right represent time steps of 10 ms

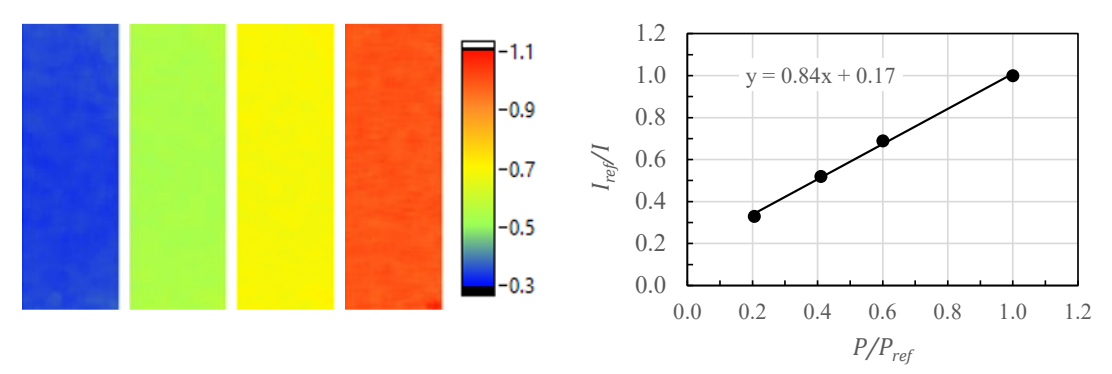


Figure 8. Intensity ratio contour (left) for $P/P_{ref} = 0.20$, 0.41, 0.61 and 1.00 and corresponding Stern-Volmer plot (right) for blue LED excitation: thick beam

Strain response: Figure 9 is a plot of the intensity ratio $\overline{I_{r,ref}}/\overline{I_r}$, OSR, and phase (G) recorded with polarized red LED excitation at $P/P_{ref} = 0.41$. Again, the reference state is atmospheric pressure and at rest. Images from left to right represent time steps of 10 ms. The intensity ratio (top row) varies relative to time and location. Unlike the emission (luminescence) process of the PSP to the blue LED excitation, the PEC is a reflection process of the red LED excitation. Thus, as the beam moves back and forth, changing its proximity and surface orientation relative to the camera, more or less light is recorded by the camera. However, the strain information is not recorded in the average of the superpixel intensity but the relative variation in the superpixel intensity to the average superpixel intensity (Eq. 10). The OSR (middle row) indicates a change in the maximum shear strain from image to image (as the beam vibrates) as well as from top to bottom. As oriented in the image, the beam is clamped at the top, and the free end is at the bottom. As the beam is driven by the shaker, the region nearer the clamped end exhibits a higher OSR (or strain) than the free end. The phase plot (bottom row) correlates with the OSR images. As the beam vibrates, the surface is alternating between states of compression and tension. The beam is oriented to the camera such that the 0° pixel is aligned with the length of the beam. For this simple beam configuration, when the phase measures 0, then the side of the beam facing the camera is in tension. And when the phase measures $\pm \pi/2$, the side of the beam facing the camera is in compression. As the beam transitions between tension and compression, the corresponding OSR response decreases (blue tones) and the phase contour transitions between 0 (blue) and $\pm \pi/2$ (red). At instances of low strain, the phase plots become more random indicating a noise floor and the transition between tension and compression.

At the LED trigger rate, about 4 images are captured per beam oscillation (tension-compression cycle). Figure 10 is a plot of the OSR at the circle locations indicated in Fig. 9. Overlaid on the OSR measurements is a rectified sinusoidal fit to the experimental data, indicating the time-dependent OSR. The OSR is always considered positive (it is a measure of the maximum shear strain—the diameter of the Mohr circle). Peaks alternate between tension and compression as indicated by the phase value in Fig. 9. Based on the fit in Fig. 10, the peak OSR per cycle is estimated. Due to coating reinforcement, the PEC fringe order must be corrected for PEC reinforcement (stiffening) and thickness gradient effects [15]. These effects become a greater factor as the ratio of coating-to-specimen thickness or modulus of elasticity increases. For the thickness ratio and material properties of this test, $N_{corr} = 0.87N$. Plotting the maximum shear strain for the four pressure tests versus the corrected fringe order, Fig. 11, yields an *in situ* calibration of η . Due to the design of the pressure seal around the shaker arm, the arm amplitude is a function of pressure, yielding lower peak strains at lower chamber pressures given the same drive signal. The *in situ* value of 925 is larger than the predicted *a priori* value of 645, indicating an interference or over-estimation of a system parameter such as the coating sensitivity, K. Finally, Fig. 12 is a plot of the relative strain, γ/η , along the length of the beam at various positions in the cycle. As expected, the strain decreases from the clamped end towards the free end due to the inertial loading of the vibrating specimen.

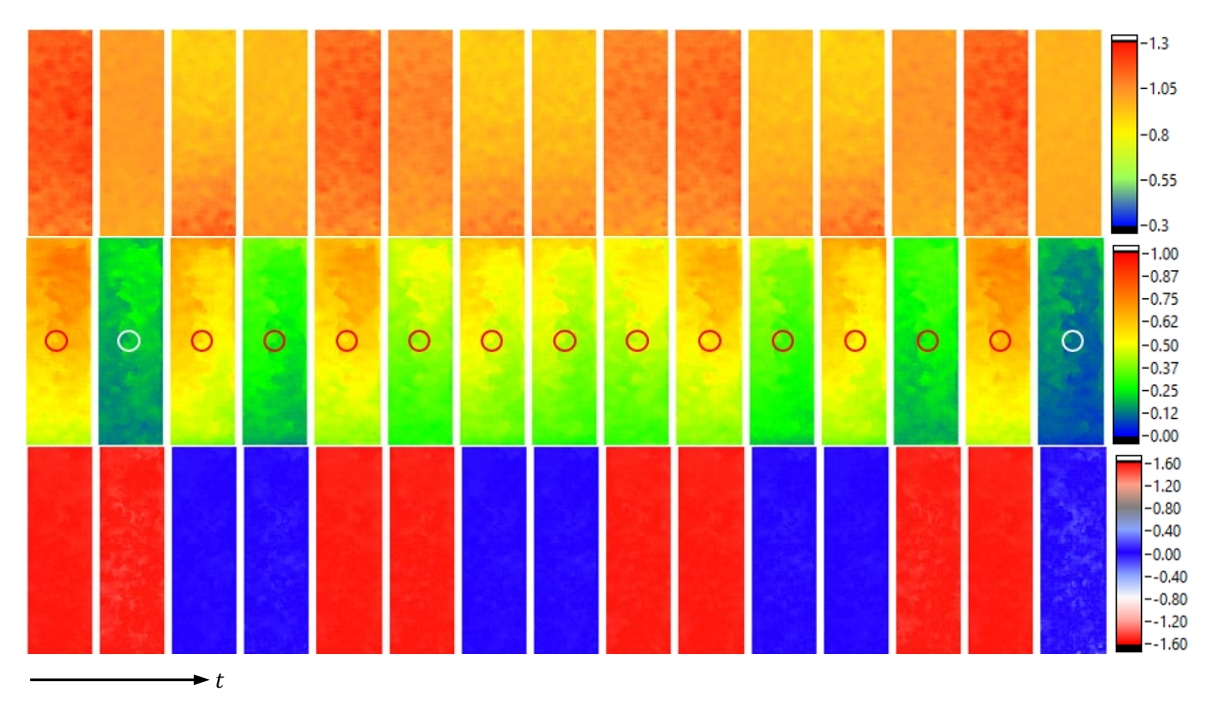


Figure 9. Intensity ratio $\overline{I_{r,ref}}/\overline{I_r}$ (top row), OSR (middle row), and phase G (bottom row; radians) recorded for the polarized red LED excitation at $P/P_{ref} = 0.41$: thick beam driven at 23.5 Hz, images from left to right represent time steps of 10 ms

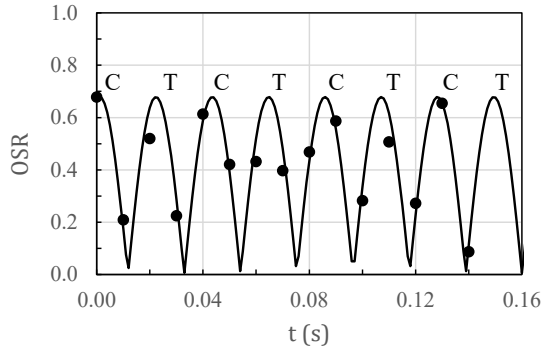


Figure 10. Measured OSR (symbol) and theoretical time-dependent fit (line): thick beam, $P/P_{ref} = 0.41$

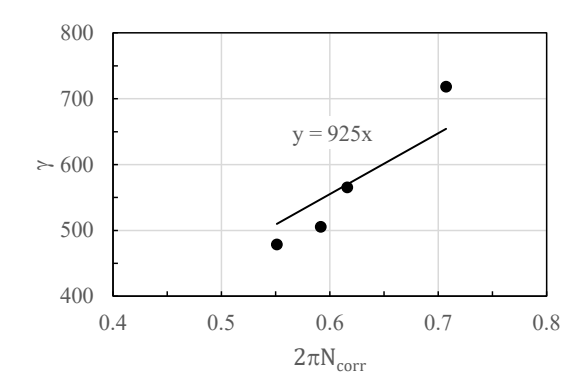


Figure 11. Maximum shear strain calibration of the PEC response: thick beam

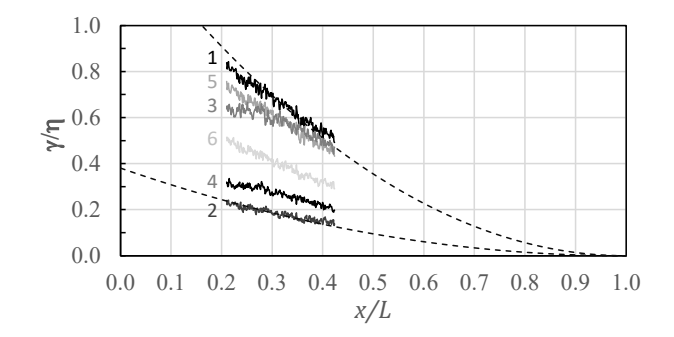


Figure 12. Relative strain along the beam centerline for the first six measurements of Fig. 10; dashed lines represent theoretical strain assuming no phase lag or damping

Similar pressure and strain results (Figs. 13-16) were recorded for the thin beam. The thin beam specimen was driven at a lower frequency, 16.2 Hz, to avoid peak resonance and limit the induced strain. The camera was triggered at 196 Hz. Pixel density was 5.9/mm. Data was acquired at four chamber pressure ratios: 0.20, 0.41, 0.61 and 1.00. For the thickness ratio and material properties, $N_{corr} = 0.82N$. Figure 13-16 summarizes the results in a similar fashion presented for the thick beam. Values of PSP and PEC sensitivities B and η , respectively, were within 5% of the thick beam results.

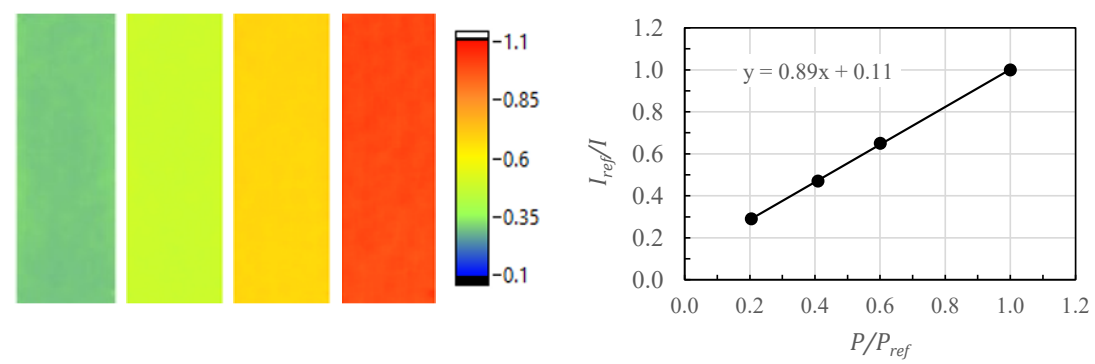


Figure 13. Intensity ratio contour (left) for $P/P_{ref} = 0.20$, 0.41, 0.61 and 1.00 and corresponding Stern-Volmer plot for blue LED excitation: thin beam

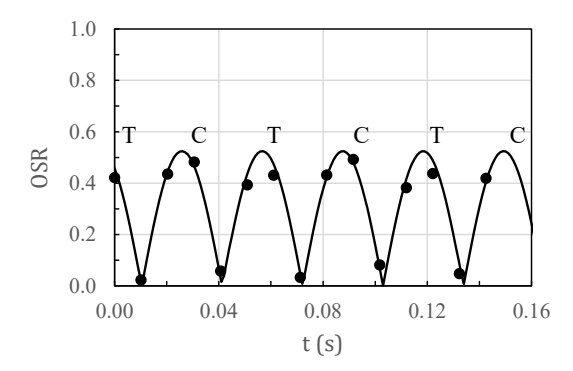


Figure 14. Measured OSR (symbol) and theoretical time-dependent fit (line): thin beam, $P/P_{ref} = 0.41$

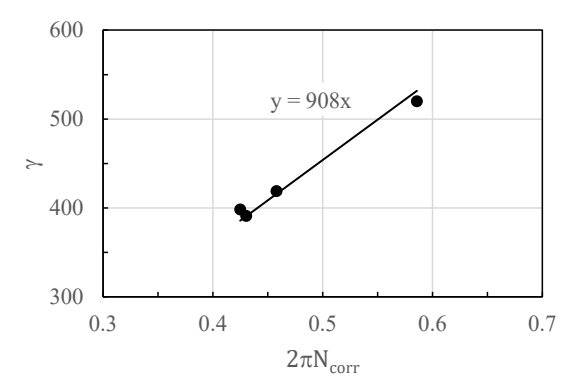


Figure 15. Maximum shear strain calibration of the PEC response: thin beam

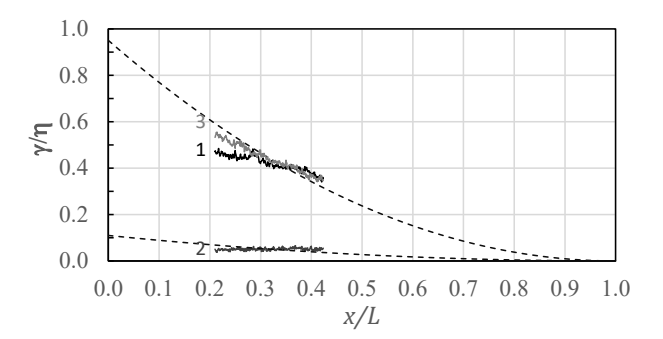


Figure 16. Relative strain along the beam centerline for the first three measurements of Fig. 14; dashed lines represent theoretical strain assuming no phase lag or damping

V. Flap Test: Facility and Initial Results

As progress continues with benchtop testing to assess and refine system response and test techniques, the research is transitioning towards high-speed application to aerodynamic environments. Currently, a test has been designed to perform in the UA Mach 3 supersonic wind tunnel, Fig. 17. The blowdown facility has a $76 \, mm \times 76 \, mm$ test section. Stagnation pressure and temperature is nominally between 480 - 540 kPa and 300 K (all pressures absolute unless stated otherwise). The tunnel has optical access on the side wall. A generic flap, Fig. 18, has been designed and fabricated to install into the sidewall across from the window (108 mm diameter). Different sized attachment plates allow flaps of various thicknesses to be installed, ranging from 1.6 mm (deforms) to 4.8 mm (effectively rigid). Each flap extends into the flow at an angle of 12°; the length of the upstream (windward) surface is 60 mm for all four flaps. The flap width is 57 mm and is expected to create a three-dimensional (3D) field.

To determine flap thicknesses that would exhibit a range of elastic deformation, preliminary calculations were conducted. The flow was assumed to be 2D and inviscid to simplify the estimation. Oblique shock and



Figure 17. UA Mach 3 supersonic wind tunnel

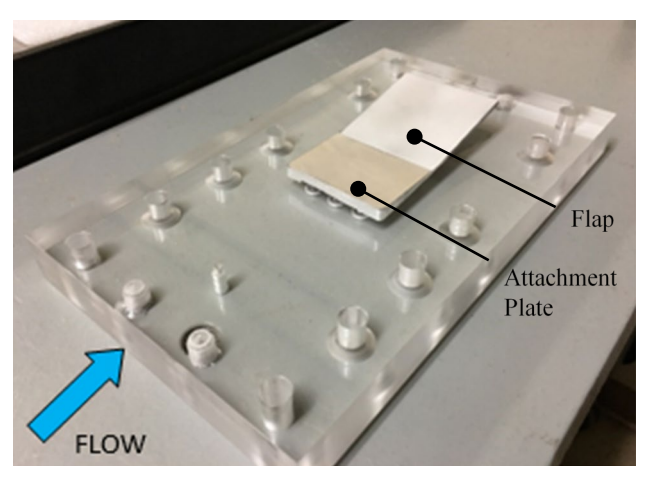


Figure 18. Side wall and surface flap for supersonic flow testing

expansion wave theory (Fig. 19) and a CFD analysis using Fluent (Fig. 20) was performed [18]. The CFD also provided an estimate of the expansion wave angle at the flap trailing edge and the corresponding flow reattachment angle which is necessary for closure of the first approach. Elastic beam theory was used to estimate the beam deflection and surface strain from the net pressure field predicted by both flow approaches. Results predicted a ~1.3 mm deflection at the trailing edge and a maximum principal strain of ~1400 $\mu\varepsilon$ (above Point A near the base of the 1.6 mm flap, Fig. 19). For the thickest flap, a ~0.01 mm deflection and a principal strain ~75 $\mu\varepsilon$ was calculated. These principal strains correspond to maximum shear strains of 1900 $\mu\varepsilon$ and 100 $\mu\varepsilon$, respectively. Initial runs without surface coatings confirmed visual deflection of the thinnest flap and no visible deflection of the thickest flap. While some minor flow contamination and surface scarring was present, longer purging runs cleared the flow environment.

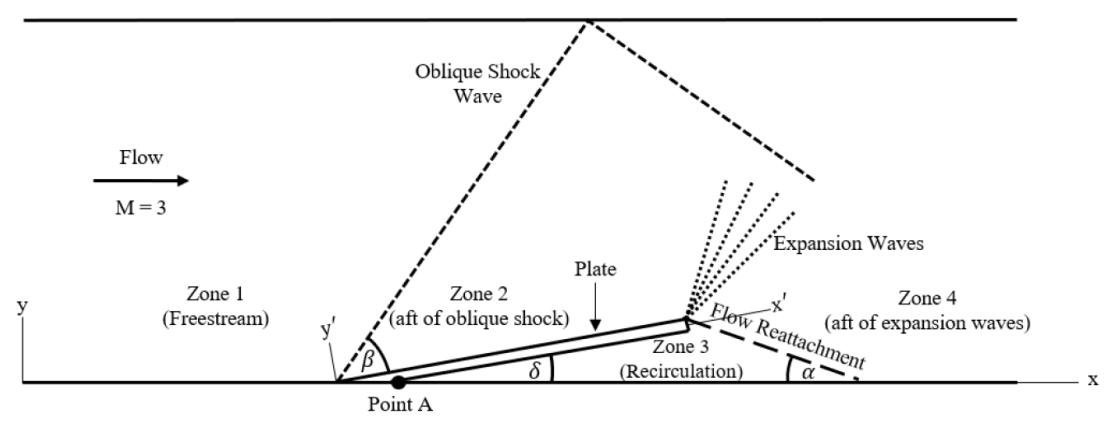


Figure 19. Schematic of the flow environment for a 2D flap

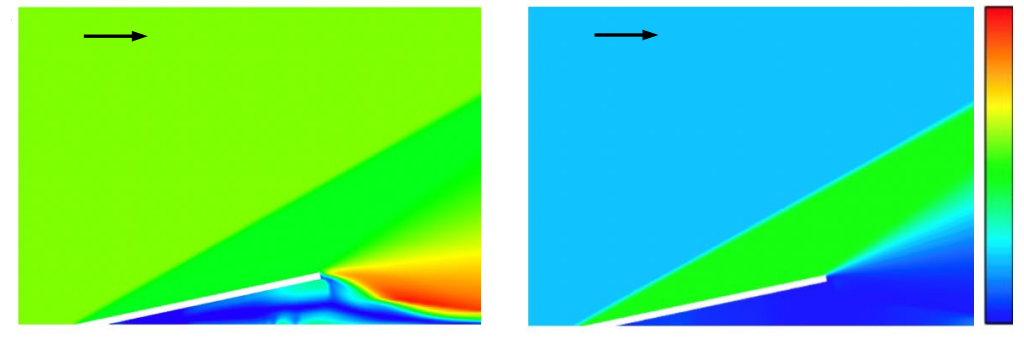


Figure 20. Inviscid, 2D Mach (left) and pressure (right) fields over the flap in M = 3 flow; M color legend: 0 to 5, P color legend: -105 to -30 kPa, g [18]

PEC-only Test: To test the PEC in the flow environment, a 60 mm \times 57 mm strip of PEC (Micro-Measurement's PS-1; h = 0.51 mm) was adhered with PC-10C adhesive on the portion of the flap surface exposed to the oncoming supersonic flow. Each flap attachment plate was designed considering the coating thickness, attempting to minimize the gap at the sidewall-flap junction. Only the 1.6 mm and 4.8 mm flaps were tested. Fig. 21 shows the OSR for the two flaps. Clearly, the thin flap shows greater strain (red area). The peak strain is downstream of the leading edge. This is to be expected as the fixed constraint is on the leeward (underneath) side of the flap (Point A in Fig. 19) for the applied pressure load. The greater pressure on the windward surface causes a downward flap deflection and a state of tension (phase map not shown). The strain decreases near the free end of the trailing edge. The strain field is not symmetric, indicating some minor flow irregularity or model misalignment of the 3D flap. The

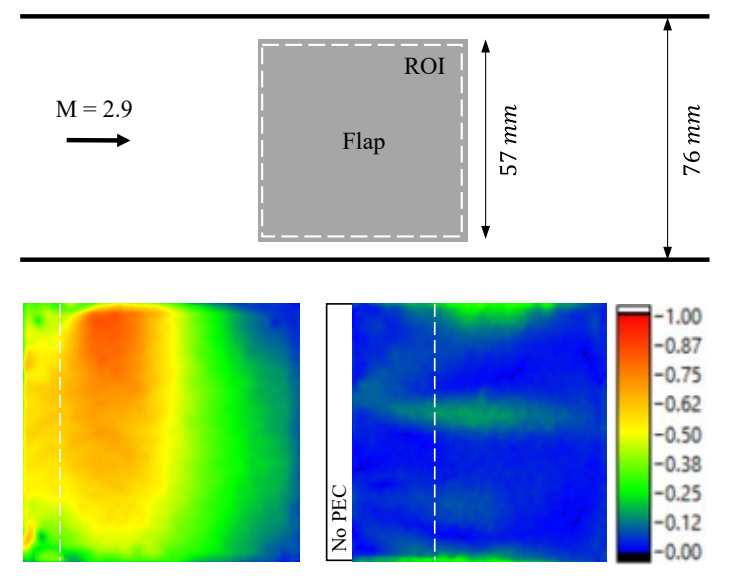


Figure 21. OSR field of the thin (left) and thick (right) on the windward side of flaps; dash line represents sidewall contact point underneath the flap

maximum shear strain of $\sim 800~\mu\varepsilon$ is less than half of the estimated value on the theoretical 2D flap in inviscid flow, indicating pressure relief due to the gaps along the side of the 3D flap. The maximum shear strain for the thick flap is under 150 $\mu\varepsilon$, and the profile shows a small spanwise variation. Figure 22 shows the time-dependent development of strain (thus deformation) on the 1.6 mm flap during start-up. Each image corresponds to a 20 ms time step.

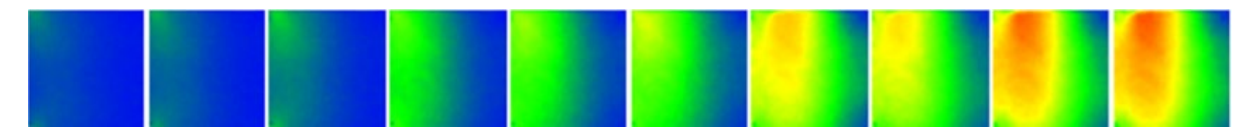


Figure 22. Time-dependent OSR of the thin flap during tunnel start: time step = 20 ms

PSP-only Test: Prior to the closing of campus research labs in early March due to the Covid-19 pandemic, two PSP-only runs were completed. Tests were performed on the 1.6 mm and 4.8 mm flaps. Figure 23 shows the windward side pressure field just after tunnel start-up. Qualitatively, the pressures fields are similar, displaying an asymmetric pattern (as did the strain field). The 2D nature of the pressure field manifests from the finite width flap. A pair of weak compression shocks appear near the leading edge; the shocks are further downstream on the thick flap compared to the thin flap. Figure 24 shows the time-dependent pressure field during tunnel start-up. The time step is 10 ms. As with the strain measurements, it takes approximately 1 to 2 s for the flow structure to set.

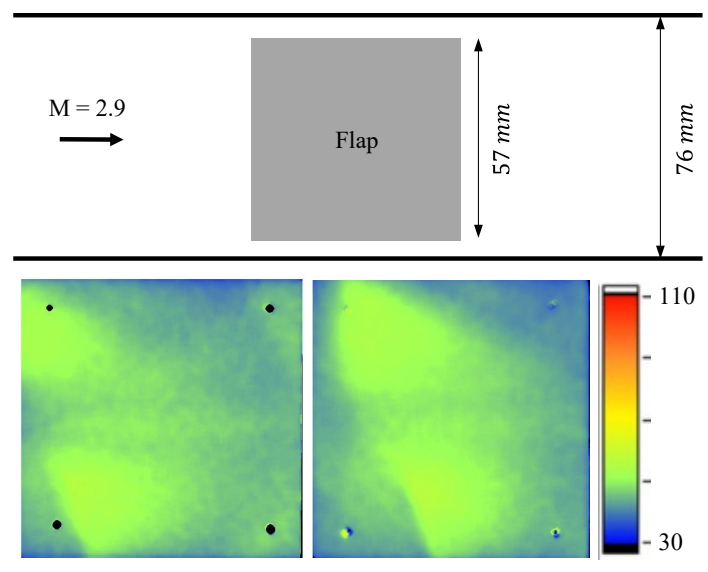


Figure 23. Pressure field (kPa) of the thin (left) and thick (right) on the windward side of flaps



Figure 24. Time-dependent pressure field on the thin (top) and thick (bottom) flap during tunnel start: time step = 10 ms

VI. Conclusions

The theory modeling the response of a dual-layer coating with pressure-sensitive paint applied on top of a photoelastic coating is presented for a dual-LED excitation approach. An unpolarized, blue LED excitation is used for the PSP and a circular polarized, red LED excitation is used for the PEC. Experimental results on a vibrating cantilever beam demonstrated that both the pressure and maximum shear strain are related to the average and standard deviation across superpixel polarization states, respectively. Pressure and strain can be quantified using appropriate analysis procedures associated with each technique. Frame rates were limited to 200 fps but could be theoretically increased with more or higher-powered excitation sources. Preliminary tests on an inclined flap in supersonic flow were initiated but then halted due to the Covid-19 pandemic. Individual PEC and PSP results show the ability to detect time-dependent surface strain and pressure, independently, during tunnel start-up. Dual-mode measurements are planned upon return to the tunnel facility.

Acknowledgments

This project is supported by NSF and AFOSR Grant CBET-1802994. The authors would like to thank ISSI and Dr. Jim Crafton with assistance in developing PSP application techniques to PEC samples and discussion of testing techniques, Mr. Easton Davis for his contribution on the theoretical calculation of the 2D flap deformation, and Ms. Kimberly Lowndes for her contribution on the new window design for the benchtop calibration chamber. Ms. Lowndes was supported by an NSF REU Site program: EEC-1659710.

References

- [1] Chism, K, J Kawell and JP Hubner, "Luminescent Measurement Technique for Analysis of Static and Dynamic Pressure and Strain Fields," AIAA Paper 2019-3150, June
- [2] Liu, T, and JP Sullivan, Pressure and Temperature Sensitive Paints, Springer-Verlag, Berlin, 2004
- [3] Crafton, J, A Forlines, S Palluconi, KY Hsu, C Carter, and M Gruber, "Investigation of Transverse Jet Injections in a Supersonic Crossflow Using Fast-Responding Pressure-Sensitive Paint," *Experiments in Fluids*, 56(27), 2015, DOI 10.1007/s00348-014-1877-3.
- [4] Flaherty, W, TM Reedy, GS Elliott, JM Austin, RF Schmit, and J Crafton, "Investigation of Cavity Flow Using Fast Response Pressure Sensitive Paint", *AIAA Journal*, **52**(11):2462-2470, 2014.
- [5] Gregory, JW, K Asai, M Kameda, T Liu, and JP Sullivan, "A Review of Pressure-sensitive Paint for High Speed and Unsteady Aerodynamics," Proceedings of the Institution of Mechanical Engineers, Part G, Journal of Aerospace Engineering, 222(2):249-290, 2008.
- [6] Casper, KM, JL Wagner, SJ Beresh, RW Spillers, and JF Henfling, "Study of Fluid-Structure Interactions on a Tunable Store in Complex Cavity Flow," AIAA Paper 2017-3125, June 2017.
- [7] Spottswood, SM, T Eason and TJ Beberniss, "Full-Field, Dynamic Pressure and Displacement Measurements of a Panel Excited by Shock Boundary-Layer Interaction," AIAA Paper 2013-2016, May 2013.
- [8] Zandman, FS, Redner, and JW Dally, Photoelastic Coatings, Iowa State University Press, Ames, IA, 1977.
- [9] Dally, J, "An Introduction to Dynamic Photoelasticity," Experimental Mechanics, 20(12):409-416, 1980.
- [10] Lesniak, JR, and MJ Zickel, "Applications of Automated Grey-field Polariscope," *Proceedings of Society of Experimental Mechanics*, 298-301, June 1998.
- [11] Hubner, JP, L Chen, Y Liu, K Schanze, J Nicolosi, P Ifju, and W El-Ratal, "Characterization of a New Luminescent Photoelastic Coating," *Experimental Mechanics*, **45**(2):137-143, 2005,
- [12] Chen, L, PG Ifju, JP Hubner, and J Nicolosi, "Full-field Strain Analysis of Composite Structures using Luminescent Photoelastic Coatings," ASC/ASTM-D30 Joint 19th Annual Technical Conference, October 2004.
- [13] Esirgemez, E, and JP Hubner, "Luminescent Photoelastic Coating Image Analysis and Strain Separation on a Three-dimensional Grid," *Optical Engineering*, **49**(8)
- [14] Hua, SQ, and Y Luo, "Improvement of the Coating Formulation in Luminescent Photoelastic Coating Method," *Experimental Techniques*, **37**(4):19-24, 2013.
- [15] Tech Note TN-706-1, "Corrections to Photoelastic Coating Fringe-Order Measurements," Micro-Measurements, Rayleigh, NC, August 2015.
- [16] Zecchino, M, PolarViewTM User Manual, 4D Technology Corporation, Rev. 2.3.0.0 A, Tucson, AZ, June 2017.
- [17] "Porous, Fast Responsive Pressure Sensitive Paint: FP-XXX," Innovative Scientific Solutions, Inc., Dayton, OH, n.d.
- [18] Davis, ER, "Stress and Strain Analysis of a Flap in Supersonic Flow," Culminating experience report for The University of Alabama MSAEM program, April 2020.